



Direct visualization of bottlebrush polymer conformations in the solid state

Jonathan M. Chan^a, Avram C. Kordon^a, Ruimeng Zhang^a, and Muzhou Wang^{a,1}

^aDepartment of Chemical and Biological Engineering, Northwestern University, Evanston, IL 60208

Edited by David A. Weitz, Harvard University, Cambridge, MA, and approved August 24, 2021 (received for review May 22, 2021)

Although the behavior of single chains is integral to the foundation of polymer science, a clear and convincing image of single chains in the solid state has still not been captured. For bottlebrush polymers, understanding their conformation in bulk materials is especially important because their extended backbones may explain their self-assembly and mechanical properties that have been attractive for many applications. Here, single-bottlebrush chains are visualized using single-molecule localization microscopy to study their conformations in a polymer melt composed of linear polymers. By observing bottlebrush polymers with different side chain lengths and grafting densities, we observe the relationship between molecular architecture and conformation. We show that bottlebrushes are significantly more rigid in the solid state than previously measured in solution, and the scaling relationships between persistence length and side chain length deviate from those predicted by theory and simulation. We discuss these discrepancies using mechanisms inspired by polymer-grafted nanoparticles, a conceptually similar system. Our work provides a platform for visualizing single-polymer chains in an environment made up entirely of other polymers, which could answer a number of open questions in polymer science.

bottlebrush polymers | super-resolution microscopy | single molecules

The foundation of our understanding of the physical behavior of polymers is derived from the behavior of single chains. For example, self-consistent field theories (SCFT) solve for the statistics of single-chain conformations in a field of surrounding polymers (1), explanations of viscoelastic properties are derived from single-chain dynamics in the presence of entanglements (2), and crystallization theories in bulk polymers are based on chain-folding models (3). Though these theories rely on the validity of our understanding of single-chain behavior, a definitive and conclusive picture of chains in a bulk material has not been acquired experimentally. It is surprising that direct visualizations of these systems elude us, as polymer melts are ubiquitous systems that form a countless number of everyday materials. Most of our knowledge of single-chain conformations is derived from small-angle scattering, though the indirect nature of these techniques requires model fitting and averaging over ensembles (4–6). Direct imaging has been successful using DNA as a model polymer, though these systems explore polymer solutions, which may not precisely reflect the conditions in a solid material (7, 8). Even though one of the first chapters of many polymer textbooks describes the conformation of polymers (2, 9, 10), to our knowledge, there has still not been a clear and convincing image of a single chain within a bulk polymer material.

The direct visualization of chains would be especially valuable for bottlebrush polymers, which have been widely explored for applications including electronics (11, 12), drug delivery (13), photonics (14, 15), and biomedical materials (16, 17). It is widely expected that bottlebrush chains adopt elongated conformations due to the steric repulsion between side chains on their densely grafted backbones (18). These conformations explain many of the key properties of bottlebrush-based materials (16, 19–26), which make them ideal candidates for applications in medical implants (20), pigments (22), and lubricants (27). However, several

studies have provided an inconsistent depiction of chain rigidity for bottlebrush polymers. For example, the self-assembly of ABC bottlebrush triblock terpolymers has been consistent with a high degree of bending and looping of the midblock (28). Similarly, work with small-angle X-ray scattering and SCFT in lamellae-forming diblock copolymer systems have suggested that rigid conformations appear at the interfaces between lamellae, but chains are much more flexible in the middle of domains (29). With little evidence to support theories connecting conformation to macroscopic properties and with conflicting hypotheses of bottlebrush rigidity, direct imaging of single chains in the solid state fills a crucial gap in our understanding of bulk bottlebrush systems.

Various techniques have been used to study bottlebrush conformations in different systems. Atomic force microscopy (19, 30) has been successful in studying single chains adhered to substrates, but these techniques are designed to only image surfaces and do not probe polymer melts in their native environments because they lack sufficient contrast between otherwise identical chains. Similarly, transmission electron microscopy (TEM) (31, 32) has been useful in imaging bottlebrushes but requires invasive sample preparation and high-vacuum environments. Cryo-TEM has successfully imaged dendronized linear polymers in solution, but applying this to bulk materials would be challenging, as it is not designed to image in this mode (33). Helium ion microscopy has successfully imaged bottlebrush chains, but this technique is still restricted to imaging surfaces and requires plasma etching to observe chains below the surface (34). Small-angle neutron scattering (SANS) has provided insight into bottlebrush chains within solutions, but this indirect characterization technique requires model fitting and does not

Significance

This work provides a clear and convincing picture of a polymer chain surrounded by other polymers in the solid state over 100 y after the molecular definition of polymers was first proposed. We achieve this feat using super-resolution optical microscopy, which provides resolution sufficient for the nanoscale detail and provides contrast of individual chains from the surrounding background through fluorescent labeling. We measure the conformation of these polymers directly from their images and show that their rigidity is significantly different from that in solution. Further analysis investigates the dependence of conformation on various parameters, such as polymer branching and the features of the surrounding polymers.

Author contributions: J.M.C. and M.W. designed research; J.M.C. and A.C.K. performed research; J.M.C. and R.Z. contributed new reagents/analytic tools; J.M.C. and M.W. analyzed data; and J.M.C. and M.W. wrote the paper.

The authors declare no competing interest.

This article is a PNAS Direct Submission.

Published under the PNAS license.

¹To whom correspondence may be addressed. Email: mwang@northwestern.edu.

This article contains supporting information online at <https://www.pnas.org/lookup/suppl/doi:10.1073/pnas.2109534118/-DCSupplemental>.

Published October 1, 2021.

provide information on single chains, as information is averaged over the entire sample (32, 35, 36).

Although these studies have provided a wealth of information, an image of a bottlebrush polymer in a bulk system has not been shown, possibly due to limitations in current techniques. An ideal technique would image at sufficient resolution, provide contrast between single chains, probe under the surface for bulk properties, and be optimized for the native environment of the polymer. Super-resolution microscopy satisfies all of these requirements (37–39). Although it has historically been used in the biological community, it has more recently made considerable insights in soft materials and polymers, such as observing micelle formation (40), visualizing crosslinker density in polymer networks (41), and studying nanoscale morphologies of block copolymer systems (42). For bottlebrush polymers, super-resolution is an especially well-suited technique, because their size and extended conformations perfectly match the resolutions (of order 10^1 nm) of these methods. Here, we use single-molecule localization microscopy (SMLM) to directly visualize single-bottlebrush polymers within melts and analyze their conformations to measure their persistence lengths.

In this study, we investigate the behavior of bottlebrush chains in a bulk system by studying films composed of linear polymer/bottlebrush polymer mixtures. We image individual bottlebrush chains using SMLM, resolve the conformations of individual bottlebrush polymers, and determine their persistence lengths (Fig. 1). After extensive analysis and simulation to confirm the accuracy and precision of our persistence lengths, we explore scaling relationships as a function of side chain length and grafting density and discuss their underlying origins in the context of the similar system of polymer-grafted nanoparticles (PGNs). Ultimately, this work establishes a platform to directly study single-polymer chains within a bulk system and provides direct evidence of single-chain behavior through imaging.

Results and Discussion

Synthesis of Bottlebrush Polymers. In order to study bottlebrush conformations through direct imaging with super-resolution microscopy, we used a synthesis scheme that achieves two requirements: 1) a convenient method to fluorescently label the polymers for SMLM and 2) a straightforward approach to tuning the architectural parameters of the bottlebrush (side chain molecular weight M_{sc}

and grafting density z , defined as the fraction of backbone repeat units with a side chain).

To satisfy requirement 1, we selected fluorescent labels of photoswitchable diarylethenes that are activated by ultraviolet light to an “on” state, which both emits fluorescence and eventually transitions back to the “off” state under blue light. Combining both wavelengths on the sample thus achieves super-resolution in a photo-activated localization microscopy (PALM) approach (37). These fluorescent diarylethenes were prepared with vinyl moieties as previously described, enabling convenient covalent attachment through copolymerization. Based on previous work, this labeling strategy shows no major effects on the polymerization kinetics from the dye, such as early termination (37).

To satisfy requirement 2, we synthesized bottlebrush polymers using a grafting-from method (18, 36), in which side chains are grown by atom transfer radical polymerization (ATRP) from a macroinitiator, that serves as the backbone of the resulting bottlebrush. This method enables easy adjustment of M_{sc} , while holding the grafting density z and backbone length constant, by simply using the same macroinitiator in each M_{sc} series. Starting with poly(hydroxyethylmethacrylate) (Polymer Source, $M_n = 243.5$ kg/mol, $D = 1.19$), we functionalized the hydroxyl groups on every monomer using mixtures of α -bromoisobutyl bromide (BiBB) and acetyl bromide with varying ratios to tune the fraction of ATRP initiation sites along the backbone, thus varying z (Fig. 2). After synthesizing the macroinitiator, we copolymerized methyl methacrylate (MMA) and the functionalized photo-switchable diarylethene directly from the backbone to form the bottlebrush polymer. Three different backbones were synthesized for grafting densities, $z = 0.08, 0.40,$ and 1 , and each backbone was incorporated into a series of bottlebrushes with five different side chain lengths. Molecular weights of the side chains M_{sc} were determined following cleavage of the chains from the backbone. These results are consistent with the expected M_{sc} calculated from the full bottlebrush molecular weight, indicating that more than 90% of the initiation sites on the backbones successfully produced a side chain (SI Appendix). The results of these syntheses are outlined in Table 1.

In this study, the backbones were polymerized from vinyl monomers, so the $z = 1$ grafting density corresponds to one side chain for every two carbons. We also selected a $z = 0.4$ condition,

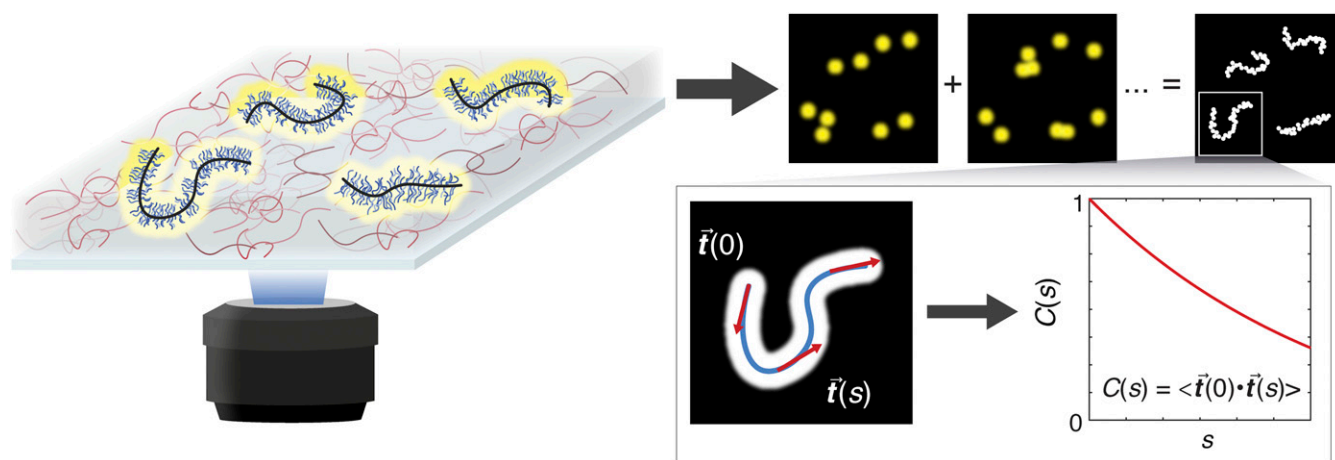


Fig. 1. Overview of using super-resolution optical microscopy to image bottlebrush polymers in the solid state. Details of the individual chains are captured by activating a small portion of the photoswitchable fluorophores that are covalently attached to the labeled bottlebrushes, which form a small fraction of the material. Although the diffraction limit of light causes these dyes to appear much larger than their actual size, their locations can be determined with much higher precision by fitting their images to the expected point-spread functions. By repeating this over many imaging frames, we can resolve pointillist images of single-bottlebrush polymers. The conformations of individual chains can then be directly analyzed, and persistence lengths l_p can be extracted from the tangent-tangent correlation function $C(s)$ averaged over an ensemble of chains.

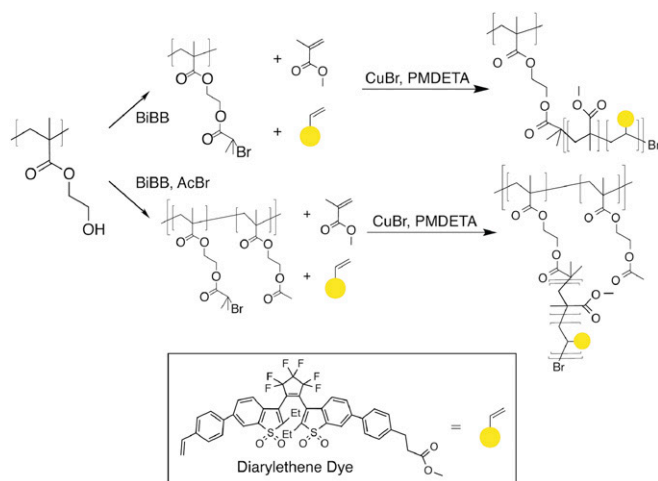


Fig. 2. Preparation of macroinitiator through reaction between poly(hydroxyethylmethacrylate) (PHEMA) and acid bromide species: α -bromoisobutyl bromide (BiBB) and acetyl bromide (AcBr). Following functionalization for the macroinitiator, side chains are polymerized by ATRP to form a statistical copolymer comprised of PMMA and a trace amount of diarylethene dye.

which may be the most relevant to the many studies of bottlebrush polymers synthesized by ring-opening metathesis polymerization (ROMP) of norbornene monomers (18, 43, 44), in which one side chain is expected for every five carbons along the backbone.

Because only a small amount of dye is used to label the bottlebrush polymers (0.25 to 0.5% by weight), we expect that the presence of dye does not affect the properties of the polymer. The body of work using fluorescence to measure polymer properties is well established (45–49). At the level of dye-labeling in our study, we sufficiently label the entire contour of the bottlebrush polymer with roughly one dye molecule for every 20 to 50 side chains or every 3 to 8 nm along the backbone. Aggregation of dyes is thus very unlikely at these concentrations. Remarkably, only a small amount of dye is required for super-resolution imaging, as shown in other examples in which concentrations of less than 1% by weight is often used for sufficient resolution (37, 50–52).

Imaging Bottlebrush Polymers in Bulk Materials. Using super-resolution microscopy, we can visualize single-bottlebrush chains in their native environment in a polymer melt, as shown in Fig. 3. In this example, the imaged sample is a 40-nm-thick film comprised of a dilute amount of dye-labeled poly(methyl methacrylate) (PMMA) bottlebrush polymer mixed with undyed linear PMMA. The linear matrix was chosen to match the composition of the side chains for chemical compatibility. A dilute concentration of dyed bottlebrush (0.3 wt% of total polymer) was used to target a substantial number of features while also avoiding overlap between neighboring bottlebrushes. A number of elongated features appear, and these features correlate relatively well to the expected average backbone contour length L_0 of our synthesized bottlebrushes of 300 nm, which is determined from the carbon-carbon bond length, bond angle, and average number of repeat units along the backbone (*SI Appendix*).

We have carefully designed our experiments to report the conformation and statistics as close to the ideal conditions of three-dimensional (3D) bottlebrushes in thermodynamic equilibrium as possible. For example, we annealed the films for 2 h at 180 °C under a nitrogen atmosphere, conditions optimized to ensure equilibrium conformations without segregation of bottlebrush chains

from the linear matrix (53). In particular, the annealing time is significantly longer than the longest relaxation time expected for similar polymers at lower temperatures, which was determined by previous linear rheology experiments to be on the order of several minutes (19, 25). We performed our experiments on 40-nm-thick films, because the whole sample fits within one \sim 100-nm focal plane of our microscope, enabling two-dimensional (2D) imaging which simplifies our procedure considerably. Thicker films can be easily used to directly capture 3D conformations using various established 3D localization techniques in SMLM (54, 55). For our 2D imaging experiments described here, because the expected average contour length $L_0 \sim$ 300 nm of the bottlebrush chains is larger than this film thickness, the backbones are assumed to adopt a mostly two-dimensional conformation parallel to the substrate. However, we do not expect confinement effects at the length scale of the side chains, as the width of the bottlebrush is on the order of single nanometers, which is much smaller than the 40 nm film thickness. As the persistence lengths are dominated by interactions of the side chains, we thus expect that these 2D images will provide an excellent measurement of backbone rigidities for a 3D melt system. We have verified this by performing Monte Carlo simulations of worm-like chains (WLC) confined in thin films. If the bending potential of the backbone (capturing side chain interactions) is unchanged for chains of increasing confinement, our simulations show that the average persistence length under confinement is identical to that in unconfined 3D chains. These results are detailed in *SI Appendix*, Fig. S19.

From the super-resolution images, relevant features were individually chosen for analysis by first finding features with a maximum Feret diameter above 200 nm and manually screening for chain-like features. Further details of this procedure are described in *SI Appendix*. In order to approximate the backbone, a trace of the elongated features was found by skeletonization analysis, which extracts the center pixels of an object in a binarized image (Fig. 4). To quantify the rigidity of an ensemble of chains within a single sample, the skeletonized traces of 350

Table 1. Bottlebrush polymer molecular weights

Bottlebrush*	$M_{n,sc}$ (g/mol) [†]	D_{sc}	Theoretical grafting density, z^{\ddagger}	$M_{n,bb}$ (kg/mol) [§]
1	640	1.1	1	1,380
2	1,100	1.31	1	2,240
3	2,030	1.22	1	3,980
4	2,860	1.22	1	5,540
5	3,500	1.27	1	6,730
6	2,830	1.33	0.4	2,390
7	3,300	1.23	0.4	2,730
8	4,940	1.59	0.4	3,960
9	5,800	1.52	0.4	4,600
10	6,550	1.6	0.4	5,160
11	1,300	1.1	0.08	501
12	3,120	1.23	0.08	774
13	4,320	1.35	0.08	953
14	5,200	1.22	0.08	1,080
15	6,180	1.35	0.08	1,230

*Each polymer was synthesized from a macroinitiator with a degree of polymerization of 1,870 and dispersity of 1.19.

[†]Side chain molecular weight as characterized by gel permeation chromatography (GPC) with multi-angle light scattering (MALS) of cleaved side chains.

[‡]Theoretical grafting density based on ¹H NMR of macroinitiators, assuming 100% initiation efficiency.

[§]Total molecular weight of bottlebrush polymer, calculated based on $M_{n,sc}$ and z .

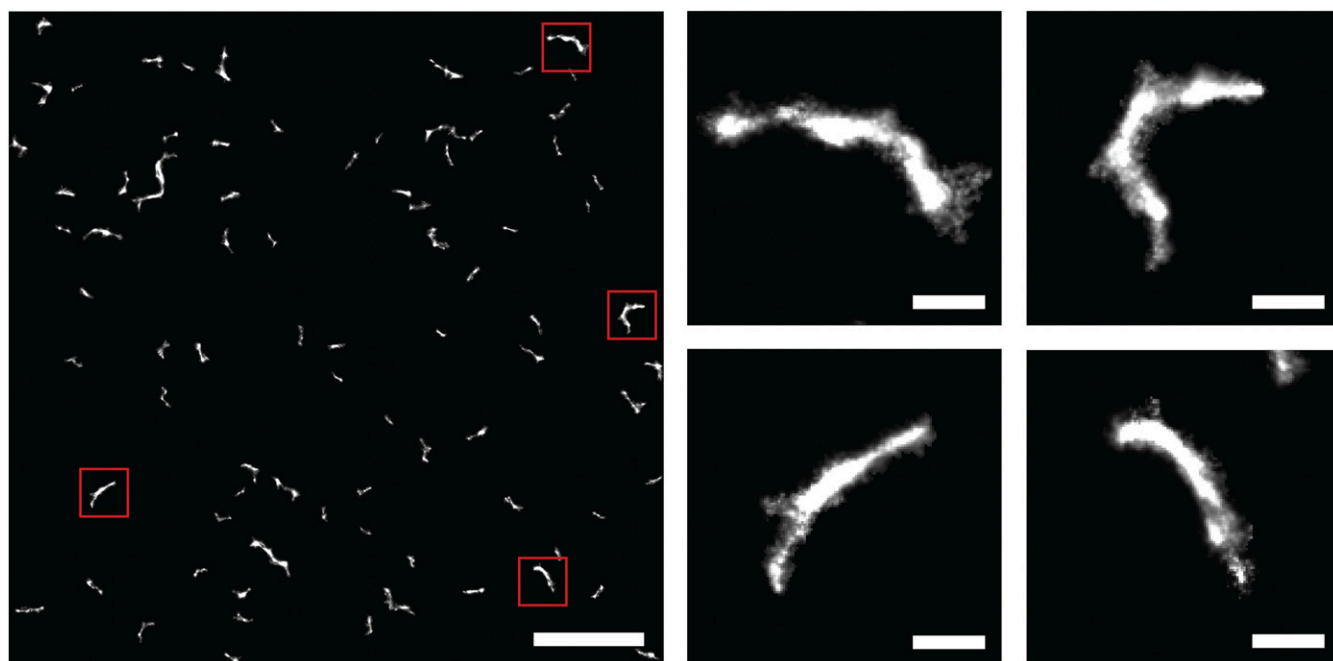


Fig. 3. Super-resolution image of dye-labeled bottlebrush polymers ($M_{sc} = 2,030$ g/mol, $z = 1$) in a matrix of linear PMMA ($M_n = 350$ kg/mol). Artifacts in the image due to fluorescent impurities have been removed to only show bottlebrush polymers within the sample, and the unprocessed image is shown in the supporting information (SI Appendix, Fig. S9). Film thickness is ~ 40 nm. (Scale bar on full image, $2 \mu\text{m}$; scale bars for zoomed sections, 200 nm.)

features from six to eight different $32 \times 32\text{-}\mu\text{m}$ areas were found, and the tangent-tangent correlation function $C(s)$ was determined for each trace. For a WLC, $C(s)$ is expected to decay exponentially,

$$C(s) = e^{-s/2l_p}, \quad [1]$$

where s is the distance along the chain and l_p is the persistence length. $C(s)$ accounts for two transverse directions in 3D, so the factor of 2 arises in the exponential constant as we reduce the number of transverse directions by half for WLCs in two dimensions (56).

Analysis of the super-resolution images show that $C(s)$ indeed follows an exponential decay, suggesting that the bottlebrush backbones are well-described by the WLC model (Fig. 5). The sharp decrease in the data observed in the first few points is an artifact that arises because the skeletonized backbone is a series of discrete points on a grid, derived from the pixelation of the underlying super-resolution image. These discrete positions

predetermine the directions of the first two tangent vectors to be parallel, perpendicular, or diagonal to each other, which affects the value of $C(s)$. This effect diminishes farther along the chain as these directions become decorrelated. Additionally, only the portion of the $C(s)$ where $s \leq 200$ is expected to decay exponentially, because we only select for chains whose contour length is larger than 200 nm, and thus, the statistics of $C(s)$ deteriorate beyond this region. In the intermediate region, $C(s)$ can be fit to exponentials to determine backbone persistence lengths l_p .

In SMLM, the position of each single-molecule event has an implicit localization uncertainty σ that is a function of the brightness of the emitter versus the background, which limits the ultimate resolution of the rendered images. In fact, the apparent width of the features is not a reflection of the actual thickness of the bottlebrushes, which is expected to be on the order of single nanometers, but rather a result of this localization uncertainty. For super-resolution images, we determined σ by measuring the distances of localizations from the skeletonized backbone (Fig. 6). These distances were plotted as a histogram and fit to a

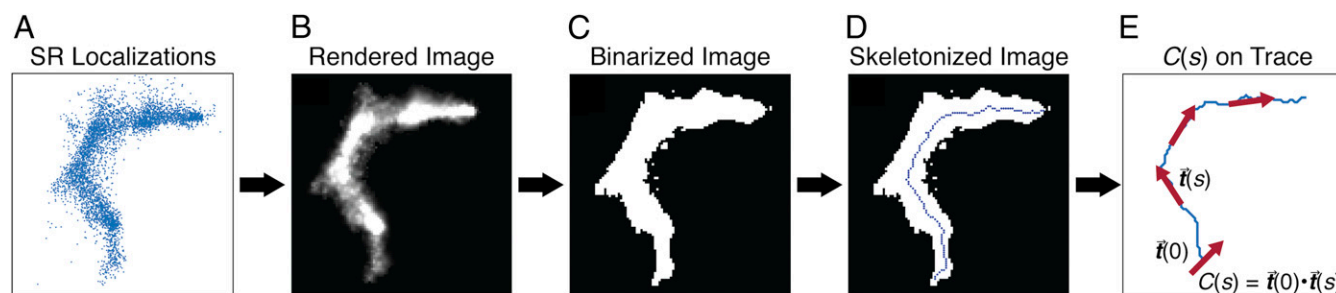


Fig. 4. Skeletonization process begins with the positions of the localized emitters (A), which are plotted in ThunderSTORM as 2D Gaussians of size given by their localization uncertainty, to form a super-resolution image (B). The image is then binarized (C) and finally skeletonized to a curve with width of one pixel (D). The curve can then be used to find the tangent-tangent correlation function $C(s)$ (E).

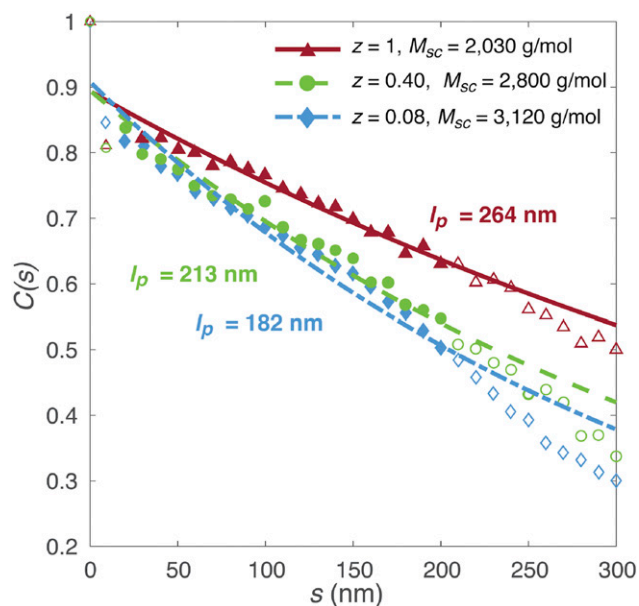


Fig. 5. Characteristic tangent-tangent correlation functions $C(s)$ for three bottlebrush polymers in a 350-kg/mol matrix. (\blacktriangle) $M_{sc} = 2,030$ g/mol, $z = 1$, (\bullet) $M_{sc} = 2,800$ g/mol, $z = 0.40$, and (\blacklozenge) $M_{sc} = 3,120$ g/mol, $z = 0.08$. $C(s)$ is fit to an exponential decay (Eq. 1) to extract a value for l_p . Only the data points with closed markers are used for fitting to avoid artifacts from pixelation at small s and poor statistics at large s .

Gaussian function, and a value of $\sigma = 11.2$ nm was determined by averaging over 20,000 localizations from 150 chains. The σ value varied minimally between different M_{sc} conditions. This noise may inhibit our ability to determine the l_p under certain ranges of L_0 and l_p .

In order to find the ranges of L_0 and l_p relative to σ that can be accurately estimated using our analysis, we simulated super-resolution images from WLCs with inputted parameters for l_p , L_0 , and σ . For ensembles of 1,000 chains under each condition, we compared the extracted persistence length $l_{p,fit}$ to the inputted persistence length $l_{p,in}$, expressed as a ratio between $l_{p,fit}$ and $l_{p,in}$ (Fig. 7). In the top left where l_p is much larger than L_0 (enclosed in blue), the resulting super-resolution images appear as elongated rods. This underestimates l_p , because an exponential fit attempted on $C(s)$ does not appreciably decay over the length of the feature. In the bottom right where L_0 is much larger than l_p (enclosed in red), the chains appear as very flexible curves, which causes some chains to loop drastically, making them difficult to accurately skeletonize. Therefore, the values of l_p are overestimated because the skeletonization removes the true bending of the chain. For much of the top right region where both l_p and L_0 are large compared to σ (enclosed in green), the chains appear as well-defined features with obvious and measurable curvature, and an accurate l_p can be determined. Given our experimental localization uncertainty of $\sigma = 11.2$ nm (Fig. 6), analyzing features of at least 200 nm in length ($L_0/\sigma > 18$) will provide reasonable estimates of backbone rigidity in the range of $l_p/\sigma \sim 16$ to 100 or $l_p \sim 180$ to 1,100 nm. This sets upper and lower bounds for the analysis of our experimental super-resolution images.

Analysis of Bottlebrush Chain Conformations. To study the effect of architecture on conformations of bottlebrush polymers, we compared the persistence lengths of different ensembles of bottlebrushes in a linear matrix of 350 kg/mol PMMA, as we varied the side chain molecular weight M_{sc} and grafting density z

of the bottlebrush polymers (Fig. 8). As expected, l_p increases as both M_{sc} and z increases. For each z condition, we find a clear power law relationship $l_p \sim M_{sc}^\alpha$, with exponents α determined to be 0.15 for $z = 1$, 0.36 for $z = 0.40$, and 0.34 for $z = 0.08$.

Conformations of bottlebrushes in a melt state have previously been explored through theoretical studies and numerical simulations, and the results of those studies have also predicted a power law relationship between l_p and M_{sc} but with an exponent of $\alpha = 0.5$ (57). The disagreement in α with our results may be explained by examining the differences between the two systems investigated: a neat system consisting entirely of bottlebrush polymers for theoretical studies and a linear-bottlebrush polymer blend in our super-resolution experiments (57, 58). Even though both the bottlebrushes and the linear matrix are composed of PMMA, the phenomenon of autophobic dewetting may apply here, where a linear polymer does not wet a polymer brush even when the chemical species are identical (59, 60). While this has been widely established for polymer-grafted nanoparticles (PGNs), we suspect that it may also apply for mixtures of linear and bottlebrush polymers under certain regimes (53, 61, 62). As previous theory and simulations of l_p in bottlebrush melts have assumed wetting conditions, autophobic dewetting may explain our deviation from these predictions.

If we extend lessons learned from PGNs to our system, the surrounding linear polymer chains would not penetrate the side chains of the bottlebrush in a dry-brush regime, due to entropic losses in this densely occupied environment compared to the freer regions far away from the bottlebrush. Instead, the side chains may adopt a collapsed conformation, similar to the case of polymer chains in a poor solvent. Steric repulsion between bulky, collapsed side chains would stretch the backbone, leading to higher persistence lengths than the tens of nanometers as found for bottlebrushes in solution (32). Additionally, scaling theories and numerical simulations have suggested that l_p of the backbone is expected to scale with the size of the side chains, because the rigidity of the bottlebrush results from repulsion between side chains and is therefore proportional to their size (57). If the side chains are ideal as hypothesized for a neat bottlebrush melt, then their radius of gyration scales as $R_{g,sc} \sim M_{sc}^{1/2}$, leading to $\alpha = 0.5$ (9). If the side chains are instead collapsed, then $R_{g,sc} \sim M_{sc}^{1/3}$ (63). While this scaling does not agree with all of the grafting densities explored in our study (Fig. 8), the influence of autophobic dewetting does support the dampened effect of side chain length (i.e., a weaker scaling than $\alpha = 0.5$).

Autophobic dewetting effects may offer additional explanations for the variation of the α scaling at different grafting

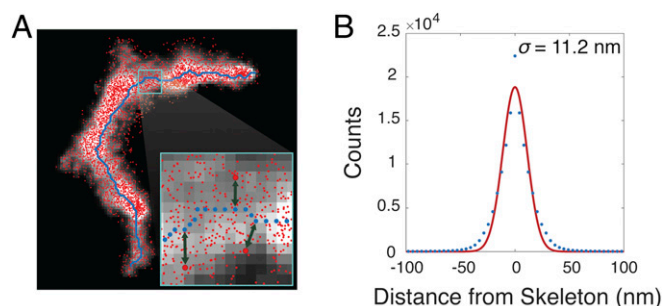


Fig. 6. Determination of localization uncertainty σ . (A) The localizations and skeletonized backbone are plotted together, and the distances between each localization and the nearest point along the backbone are determined, as shown in the *Inset*. (B) The distances of each localization from the backbone are plotted on a histogram and fit to a Gaussian function. From this fit, σ is determined to be 11.2 nm.

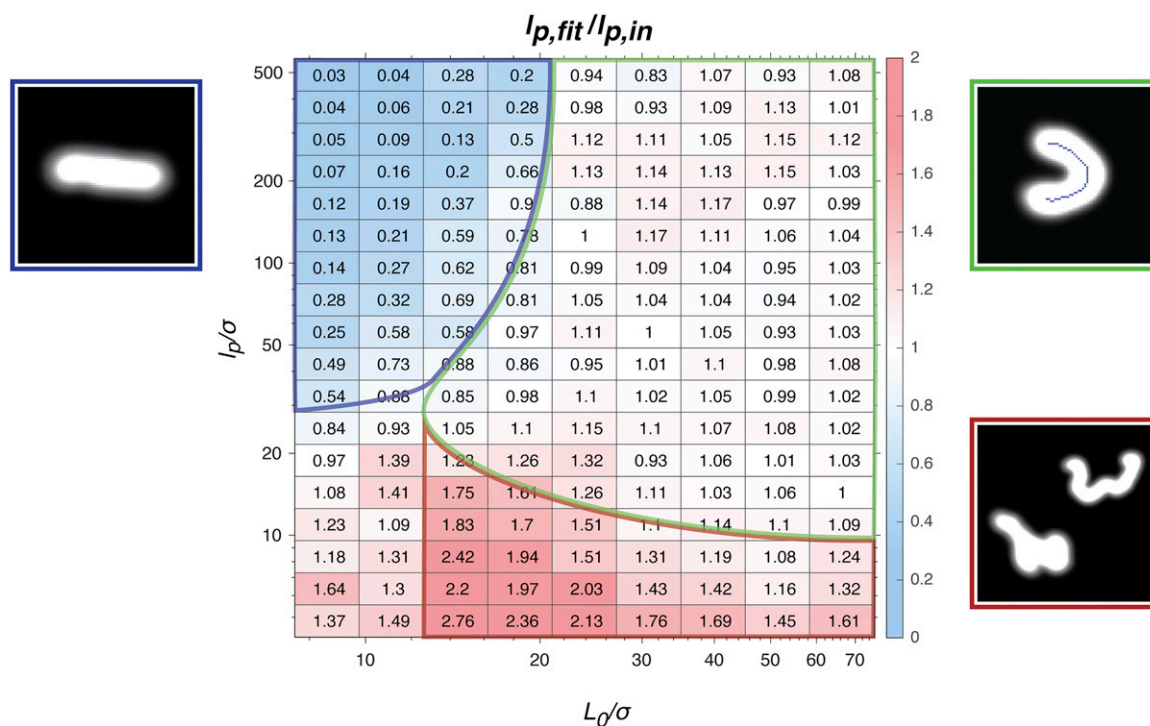


Fig. 7. Simulation of SMLM images of WLCs to probe the accuracy of estimating persistence lengths from the experimental images, over a range of contour lengths (L_0), persistence lengths (l_p), and localization uncertainties (σ). The results show a ratio between the extracted value of l_p to the l_p that was input into the simulation, shown as numbers and colored as a heat map. The blue shaded region at the top left reflects a regime in which the analysis tool poorly estimates an accurate l_p as the features all appear as rigid rods. In the region at the bottom right shaded in red, the features are more flexible, bending drastically. The green region reflects areas where the analysis tool is able to adequately skeletonize the simulated bottlebrush features and extract an accurate l_p .

densities. For PGNs in identical homopolymer matrices, penetration of the matrix polymer into the brush decreases as surface grafting density increases (Fig. 9) (59). A similar phenomenon may happen in the case of bottlebrushes. At lower grafting densities, the linear matrix may penetrate and wet the side chains of the bottlebrush polymer. In the fully grafted system, it is likely that the conformational entropy losses of the side chains exclude the surrounding chains from the vicinity of the bottlebrush, resulting in decreased wettability. Therefore, we expect the side chains to collapse, resulting in sterically bulkier groups that stiffen the backbone of the bottlebrush. This may explain the difference in the α exponent at different grafting densities, in which higher grafting densities result in dry-brush behavior, which reduces α , while the lower grafting densities allow more penetration from the matrix polymer, which brings α closer to the 0.5 exponent expected for ideal side chain conformations.

It is notable that a 2.5 \times decrease in grafting density from $z = 1$ to $z = 0.4$ causes such a dramatic change in both the values of l_p and the scaling exponent α , while a further 5 \times decrease to $z = 0.08$ shows a much smaller effect. We provide some speculation to explain this surprising result based on scaling theories. Since the persistence length should scale as the size of the side chains, the expected dependence of l_p on z can be informed by the dependence of $R_{g,sc}$ on z . As z increases, scaling theories have hypothesized that beyond a transition point $z^{**} = bl^2/v$, the molecules go from a loose-bottlebrush to a dense-bottlebrush regime (DB), in which the side chains transition from being relatively unperturbed to elongating into extended conformations. Using PMMA as our system, the Kuhn length is $b = 1.53$ nm, monomer length is $l = 0.25$ nm, and monomer volume is $v = 0.149$ nm³, leading to a transition point of $z^{**} = 0.64$ (64). This

suggests that only our $z = 1$ condition is in the DB regime, in which the extended conformations of the side chains explains the unique departure from the $z = 0.4$ and $z = 0.08$ conditions. The effect of autophobic dewetting complicates this behavior, adding uncertainty to the transition point for example, and further scaling theories or additional experimental conditions may shed light. However, this qualitative physical picture is a plausible explanation for the differing behavior of $z = 1$ versus $z = 0.4$ and $z = 0.08$.

For $z = 0.08$, we observe an outlier at the lowest M_{sc} condition. We suspect that this outlier occurs because the true l_p is outside the region where we expect to accurately measure l_p , based on our simulations (Fig. 7). If we extrapolate the $\alpha = 0.34$ relationship obtained after excluding this outlier, the expected l_p at this M_{sc} of 1.3 kg/mol is ~ 130 nm. From our simulation results (Fig. 7) with $\sigma = 11.2$ nm (Fig. 6), the true l_p is expected to be overestimated by $\sim 61\%$, which results in an estimated value for l_p of 209 nm. This approaches our result of $l_p = 206$ nm, providing a potential explanation for the anomalously high l_p that we obtained at this condition.

To better understand wet- and dry-brush effects, we measured l_p in our $z = 1$ bottlebrush series in a shorter linear matrix of 2 kg/mol, and we compared this with our previous results in the longer 350-kg/mol matrix. As shown in Fig. 10, we observe an overall decrease in l_p as well as an increase in α in the lower molecular weight linear matrix. These results may also be explained in the context of autophobic dewetting. Based on studies of PGN/homopolymer nanocomposites, the relative length of the grafted chains versus the matrix chains plays a role in determining wet/dry-brush regimes, among other factors such as grafting density as discussed above (59). When the matrix polymer surrounding

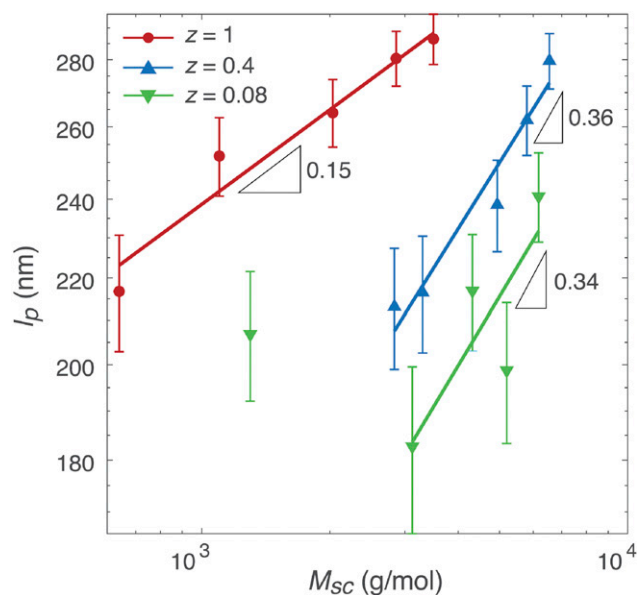


Fig. 8. Persistence length versus side chain molecular weight for bottlebrush polymers in a 350-kg/mol linear matrix for grafting densities $z = 0.08, 0.40,$ and 1 . Each point reflects data from 350 chains. Error bars represent 95% CIs, which were determined by analyzing 10 sets of 350 simulated WLCs with the experimentally measured L_o and l_p to find the SD of the average of each set. We used simulated chains to calculate the SD, because determining l_p requires first averaging $C(s)$ over many chains before fitting an exponential (Eq. 1), so directly calculating the SD over the 350 experimental chains is not meaningful.

PGNs is much larger than the grafted chains, dry-brush conditions are expected. This result is consistent with our observations for bottlebrush polymers within a linear matrix. Within a higher molecular weight matrix, we expect dry-brush conditions, which collapse the bottlebrush side chains and cause a high degree of steric repulsion that extends the backbone. This explains the higher l_p observed in the 350-kg/mol matrix. For the smaller 2-kg/mol matrix, the scaling exponent α increases in the same way as previously observed when the grafting density is lowered (Fig. 10). This result is consistent, as lowering both the matrix molecular weight and the grafting density are expected to increase the wetting of the side chains by the matrix polymers.

We observe a sharp increase in l_p at the lowest M_{sc} condition for bottlebrushes in the 2-kg/mol matrix, compared to other side chain lengths. While this increase may arise because this data point is outside the region where l_p can be accurately determined by our analysis methods, it is possible that this result reflects a transition point between wet- and dry-brush regimes. For PGNs in homopolymer matrices, dry-brush behavior dominates as the molecular weight of the grafted chains decreases (60, 65). Because the M_{sc} at this condition is the lowest compared to the matrix polymer molecular weight, a transition to a dry-brush regime may have occurred. This may explain the very similar l_p values between the two matrix molecular weights, as both are in the dry-brush regime. Although our results provide evidence of this transition, further studies, such as a deeper investigation of the effect of matrix molecular weight, are required to better substantiate this explanation.

Conclusion

We report a platform to visualize individual bottlebrush polymer chains within a bulk system using super-resolution optical microscopy. By imaging our library of synthesized bottlebrush

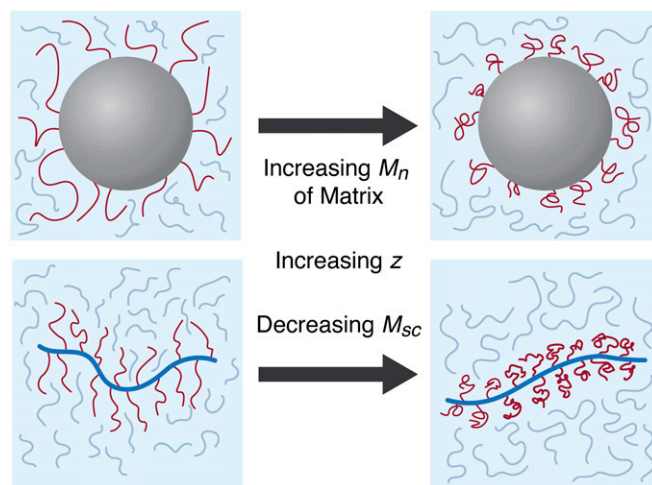


Fig. 9. The effect of autophobic dewetting for PGN and bottlebrush systems. When the molecular weight of the matrix increases, the grafting density z increases, or the side chain molecular weight M_{sc} decreases and the grafted chains transition to a dry-brush regime, causing them to collapse. For bottlebrushes, the collapsed chains increase steric repulsion, causing the backbone to become more rigid.

polymers in a matrix of linear polymer, we are capable of directly studying the conformations of single chains and extracting persistence lengths to quantify rigidity. In the analysis of our super-resolution images, we find that for each grafting density condition, there is a clear power law relationship between backbone persistence length and side chain length of the bottlebrushes. Surprisingly, our results deviate from the expected scaling relationships derived from simulation studies of bottlebrush melts. By drawing inspiration from the similar system of polymer-grafted nanoparticles, we speculate that the molecular weight mismatch between the matrix polymer and grafted side chains

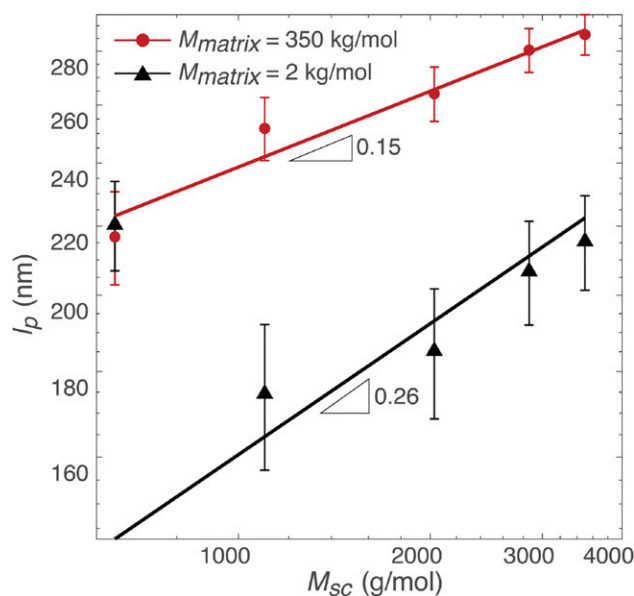


Fig. 10. l_p versus M_{sc} for fully grafted bottlebrush polymers ($z = 1$) in a 2-kg/mol and 350-kg/mol PMMA matrix. Each point reflects data from 350 chains. Error bars represent the 95% CIs, determined by analyzing 10 sets of 350 simulated WLCs with the experimentally measured L_o and l_p to find the SD of the average of each set.

causes autophobic dewetting. This explains both the higher rigidity of the backbones in comparison to SANS studies of bottlebrush polymers in solution as well as the deviation in the scaling relationships for l_p compared to bottlebrush melt simulations. Furthermore, we tested our hypothesis by studying chain conformations in a lower molecular weight matrix, and through these studies, we observe a decrease in overall l_p , as well as an increase in the scaling exponent. Overall, our study fills an obvious gap within our understanding of polymer science: the ability to directly visualize individual polymer chains in a field surrounded by other polymers. We provide a technique that may open doors in other systems to study single-chain behaviors in bulk polymer systems.

Materials and Methods

General Procedures. All materials were obtained from Sigma-Aldrich unless otherwise stated. ^1H NMR spectra were acquired using a 400-MHz Bruker Avance III HD 400 system. Molecular weight characterization of the bottlebrush polymers and cleaved side chains was performed by gel permeation chromatography (GPC) using an Agilent 1200 series system running with tetrahydrofuran as the mobile phase and two PolyPore 300 \times 7.5 mm columns (Varian p/n 5M-POLY-008-112). The instrument is equipped with 18-angle DAWN HELEOS II multiangle light scattering detector, a ViscoStar II viscometer, and a Optilab T-REX differential refractive index detector (Wyatt). We confirmed dye attachment on our polymers on a preparatory GPC system (JAI LaboACE LC5060) equipped with a UV-visible detector. To determine the concentration of dye attached on the polymer samples, we used Thermo Scientific Evolution 201 UV-visible spectrophotometer (*SI Appendix, Fig. S4*). Film thicknesses were measured by variable angle spectroscopic ellipsometer (J.A. Wollam Co., M-2000D), and the uniformity of films were verified by multiple measurements at different locations on the sample.

Synthesis of Macroinitiator. Poly(hydroxyethyl methacrylate) (500 mg, 3.8 mmol of repeat units), obtained from Polymer Source, was dissolved in pyridine (10 mL) in a round-bottom flask with a stir bar. The flask was topped with a rubber septum. For a fully functionalized backbone, α -bromoisobutyl bromide (BiBB, 4.40 g, 19 mmol) was added dropwise. To vary the grafting density of the backbone, we varied the number of bromide groups on the macroinitiator by using a mixture of BiBB and acetyl bromide instead. The reaction was stirred for 3 h in the ice bath and for an additional 20 h at room temperature. Pyridine salts were removed by vacuum filtration. The macroinitiator was precipitated in methanol and dried under vacuum to recover a product of white powder (850 mg, 79% yield). ^1H NMR spectra are shown in *SI Appendix, Figs. S1–3*, and GPC is shown in *SI Appendix, Fig. S6*.

Polymerization of Side Chains. Anisole (1.33 mL) and N,N,N',N''-Pentamethyldiethylenetriamine (PMDETA, 0.014 mL, 0.072 mmol) were added to a small, three-neck, round-bottom flask with a stir bar and degassed by three freeze-pump-thaw cycles. Copper (I) bromide (12 mg, 0.083 mmol) was quickly added under nitrogen flow during the last freeze cycle, and the vessel was placed under vacuum for 10 min and then refilled with nitrogen. In a Schlenk tube, macroinitiator (10 mg) was dissolved in anisole (1.33 mL) with MMA (420 mg, 4.2 mmol) and diarylethene dye (1 mg, 0.0012 mmol). This mixture was degassed by three freeze-pump-thaw cycles. The Cu/PMDETA solution was transferred into the solution of monomer and macroinitiator, and the reaction was stirred at 50 °C for 1 to 4 h, depending on targeted side chain length. Residual copper was removed over basic alumina, and unreacted dye was removed by preparative GPC. The polymer was precipitated in methanol and dried under vacuum to recover a white powder. The percent yield of these polymerizations was typically 15 to 25%. GPC of bottlebrush polymer and cleaved side chains can be found in *SI Appendix, Figs. S6 and S7*.

Side Chain Cleavage. To determine the molecular weight and dispersity of the side chains independently, we cleaved the side chains from the backbone by

ester methanolysis. Cleavage was performed in a glove box by dissolving bottlebrush polymer in toluene (5 mL) and adding a 1-M solution of tetrabutylammonium hydroxide in methanol (2 mL). The reaction was heated at 90 °C for 48 h. Afterward, the mixture was neutralized with hydrochloric acid, dried under vacuum, and analyzed by GPC.

Sample Preparation. Polymer films were prepared by spin-coating a polymer solution onto #1.5 thickness glass coverslips that were treated with Piranha solution (3:1 by volume of H_2SO_4 and 30% H_2O_2) for at least 3 h. The polymer solution was composed of a mixture of linear PMMA and bottlebrush PMMA (1:0.003 of linear to bottlebrush polymer by weight) dissolved in anisole. Polymer films of 40-nm thickness were annealed for 2 h at 180 °C under a nitrogen atmosphere.

Super-Resolution Optical Microscopy. The optical apparatus consists of a custom modified Olympus IX73 inverted microscope equipped with optical components from ThorLabs unless otherwise stated. All optical filters were acquired from Semrock. A 375-nm continuous-wave (CW) laser (60 mW, CrystalLaser) and a 473-nm CW laser (500 mW, Laser Quantum) were used. For the 375-nm laser, the beam was passed through a bandpass filter (LD01-375/6–12.5) to remove extraneous wavelengths, a spatial filter to clean up the beam, and a series of lenses to expand the beam. The intensity of the 375-nm laser was adjusted with a half-wave plate and polarizer, followed by a quarter-wave plate to circularly polarize the beam. The 473-nm laser was passed through a bandpass filter (LD01-473/10–12.5), a half-wave plate, and a quarter-wave plate. The two beams were combined with a dichroic mirror (Di03-R405-tl-25 \times 36) and focused to the back focal plane of an oil immersion objective (Olympus, 100 \times , 1.49 NA) to produce a collimated beam on the sample. The intensity of the 473-nm laser was 1.7 kW/cm², and the 375-nm laser was continually adjusted during the experiment to range from 0 to 85 W/cm². The emitted light from the sample was filtered through a dichroic mirror (Di03-R488-tl-25 \times 35), a bandpass filter (FF01-560/94–25), and a long-pass filter (BLP01-488R-25), and the emission ultimately was projected onto a camera (Hamamatsu, ORCA-Flash4.0 V3).

For each super-resolution image, we acquired 10,000 frames with an exposure time of 10 ms over a 32 \times 32 μm area. Under simultaneous irradiation of the 375-nm and 473-nm lasers, the dyes switch between the dark and bright states under dynamic equilibrium, and increasing power to the 375-nm laser increases the concentration of bright activated emitters. This provides an efficient handle to optimize for the highest number of emitters while also limiting the amount of overlap between neighboring emitters.

Super-resolution images were processed using a custom fitting algorithm written in MATLAB. This algorithm determined the x and y positions of each emitter by fitting point-spread functions described by 2D Gaussians using maximum-likelihood estimation (66), accounting for pixel-dependent gain values from the sCMOS camera and allowing for multiple emitters (67, 68). The positions of every emitter from all 10,000 frames were imported into the ThunderSTORM ImageJ plug-in to reconstruct and visualize a super-resolution image from these points, which plots each emitter as a 2D Gaussian with an uncertainty given by the fitting algorithm (69). ThunderSTORM's "drift correction" function was used to correct for drift in x and y, and "merge" was used to correct for emitters that appear over multiple frames by combining localizations within 20 nm of each other in consecutive frames.

Data Availability. All study data are included in the article and/or *SI Appendix*.

ACKNOWLEDGMENTS. We are grateful to Dr. Joel Sarapas and Profs. Masahiro Irie, Julia Kalow, John Torkelson, and Kenneth Shull for access to their equipment and useful discussions. We thank Prof. Zhe Qiang for preliminary work that supported this study. We acknowledge the Donors of the American Chemical Society Petroleum Research Fund and the National Science Foundation (DMR-1945249) for partial support of this research. This work made use of the Integrated Molecular Structure Education and Research Center (IMSERC) facility at Northwestern University, which has received support from the Soft and Hybrid Nanotechnology Experimental Resource (NSF ECCS-2025633), the State of Illinois, and the International Institute for Nanotechnology.

1. G. H. Fredrickson, V. Ganesan, F. Drolet, Field-theoretic computer simulation methods for polymers and complex fluids. *Macromolecules* **35**, 16–39 (2002).
2. M. Doi, S. F. Edwards, *The Theory of Polymer Dynamics* (Clarendon Press, 1988).

3. M. C. Zhang, B. H. Guo, J. Xu, A review on polymer crystallization theories. *Crystals* **7** https://doi.org/10.3390/cryst7010004. (2017).
4. R. L. Jones, S. K. Kumar, D. L. Ho, R. M. Briber, T. P. Russell, Chain conformation in ultrathin polymer films using small-angle neutron scattering. *Macromolecules* **34**, 559–567. (2001).

5. J. Kraus, P. Müller-Buschbaum, T. Kuhlmann, D. W. Schubert, M. Stamm, Confinement effects on the chain conformation in thin polymer films. *Europhys. Lett.* **49**, 210–216 (2000).
6. G. Lieser, E. W. Fischer, K. Ibel, Conformation of polyethylene molecules in the melt as revealed by small-angle neutron scattering. *Polym. Lett. Ed.* **13**, 39–43 (1975).
7. T. T. Perkins, D. E. Smith, S. Chu, Direct observation of tube-like motion of a single polymer chain. *Science* **264**, 819–822 (1994).
8. D. J. Mai, C. M. Schroeder, 100th Anniversary of macromolecular science viewpoint: Single-molecule studies of synthetic polymers. *ACS Macro Lett.* **9**, 1332–1341 (2020).
9. M. Rubinstein, R. H. Colby, *Polymer Physics* (Oxford University Press, 2003).
10. P. C. Hiemenz, T. P. Lodge, *Polymer Chemistry* (Taylor & Francis, ed. 2, 2007).
11. C. D. Heinrich, M. Thelakkat, Poly(3-hexylthiophene) bottlebrush copolymers with tailored side-chain lengths and high charge carrier mobilities. *J. Mater. Chem. C Mater. Opt. Electron. Devices* **4**, 5370–5378 (2016).
12. X. Yin, Y. Qiao, M. R. Gadinski, Q. Wang, C. Tang, Flexible thiophene polymers: A concerted macromolecular architecture for dielectrics. *Polym. Chem.* **7**, 2929–2933 (2016).
13. Y. Yu *et al.*, Well-defined degradable brush polymer-drug conjugates for sustained delivery of Paclitaxel. *Mol. Pharm.* **10**, 867–874 (2013).
14. B. B. Patel *et al.*, Tunable structural color of bottlebrush block copolymers through direct-write 3D printing from solution. *Sci. Adv.* **6**, eaaz7202 (2020).
15. M. Vatankehah-Varnosfaderani *et al.*, Chameleone-like elastomers with molecularly encoded strain-adaptive stiffening and coloration. *Science* **359**, 1509–1513 (2018).
16. M. Vatankehah-Varnosfaderani *et al.*, Mimicking biological stress-strain behaviour with synthetic elastomers. *Nature* **549**, 497–501 (2017).
17. A. N. Keith, *et al.*, Bottlebrush bridge between soft gels and firm tissues. *ACS Cent. Sci.* **6**, 413–419 (2020).
18. R. Verduzco, X. Li, S. L. Pesek, G. E. Stein, Structure, function, self-assembly, and applications of bottlebrush copolymers. *Chem. Soc. Rev.* **44**, 2405–2420 (2015).
19. W. F. M. Daniel *et al.*, Solvent-free, supersoft and superelastic bottlebrush melts and networks. *Nat. Mater.* **15**, 183–189 (2016).
20. A. N. Keith *et al.*, Bottlebrush bridge between soft gels and firm tissues. *ACS Cent. Sci.* **6**, 413–419 (2020).
21. B. R. Sveinbjörnsson *et al.*, Rapid self-assembly of brush block copolymers to photonic crystals. *Proc. Natl. Acad. Sci. U.S.A.* **109**, 14332–14336 (2012).
22. D. P. Song, T. H. Zhao, G. Guidetti, S. Vignolini, R. M. Parker, Hierarchical photonic pigments via the confined self-assembly of bottlebrush block copolymers. *ACS Nano* **13**, 1764–1771 (2019).
23. T. P. Lin *et al.*, Effects of grafting density on block polymer self-assembly: From linear to bottlebrush. *ACS Nano* **11**, 11632–11641 (2017).
24. S. W. Hong *et al.*, On the self-assembly of brush block copolymers in thin films. *ACS Nano* **7**, 9684–9692 (2013).
25. S. J. Dalsin, M. A. Hillmyer, F. S. Bates, Linear rheology of polyolefin-based bottlebrush polymers. *Macromolecules* **48**, 4680–4691 (2015).
26. I. N. Haugan *et al.*, Consequences of grafting density on the linear viscoelastic behavior of graft polymers. *ACS Macro Lett.* **7**, 525–530 (2018).
27. G. Xie, M. R. Martinez, M. Olszewski, S. S. Sheiko, K. Matyjaszewski, Molecular bottlebrushes as novel materials. *Biomacromolecules* **20**, 27–54 (2019).
28. D. F. Sunday *et al.*, Self-assembly of abc bottlebrush triblock terpolymers with evidence for looped backbone conformations. *Macromolecules* **51**, 7178–7185 (2018).
29. S. J. Dalsin *et al.*, Bottlebrush block polymers: Quantitative theory and experiments. *ACS Nano* **9**, 12233–12245 (2015).
30. E. B. Zhulina, O. V. Borisov, V. A. Pryamitsyn, T. M. Birshtein, Coil-globule type transitions in polymers. 1. collapse of layers of grafted polymer chains. *Macromolecules* **24**, 140–149 (1991).
31. S. L. Pesek, X. Li, B. Hammouda, K. Hong, R. Verduzco, Small-angle neutron scattering analysis of bottlebrush polymers prepared via grafting-through polymerization. *Macromolecules* **46**, 6998–7005 (2013).
32. S. L. Pesek, Q. Xiang, B. Hammouda, R. Verduzco, Small-angle neutron scattering analysis of bottlebrush backbone and side-chain flexibility. *J. Polym. Sci., B, Polym. Phys.* **55**, 104–111 (2017).
33. D. Messmer *et al.*, 3D conformations of thick synthetic polymer chains observed by cryogenic electron microscopy. *ACS Nano* **13**, 3466–3473 (2019).
34. N. Borodinov *et al.*, Molecular reorganization in bulk bottlebrush polymers: direct observation via nanoscale imaging. *Nanoscale* **10**, 18001–18009 (2018).
35. S. Lecommandoux *et al.*, Effect of dense grafting on the backbone conformation of bottlebrush polymers: determination of the persistence length in solution. *Macromolecules* **35**, 8878–8881 (2002).
36. J. M. Sarapas, T. B. Martin, A. Chremos, J. F. Douglas, K. L. Beers, Bottlebrush polymers in the melt and polyelectrolytes in solution share common structural features. *Proc. Natl. Acad. Sci. U.S.A.* **117**, 5168–5175 (2020).
37. Z. Qiang, K. M. Shebek, M. Irie, M. Wang, A polymerizable photoswitchable fluorophore for super-resolution imaging of polymer self-assembly and dynamics. *ACS Macro Lett.* **7**, 1432–1437 (2018).
38. M. A. Thompson, M. D. Lew, W. E. Moerner, Extending microscopic resolution with single-molecule imaging and active control. *Annu. Rev. Biophys.* **41**, 321–342 (2012).
39. D. Wöll *et al.*, Polymers and single molecule fluorescence spectroscopy, what can we learn? *Chem. Soc. Rev.* **38**, 313–328 (2009).
40. J. Yan *et al.*, Optical nanoimaging for block copolymer self-assembly. *J. Am. Chem. Soc.* **137**, 2436–2439 (2015).
41. E. Siemes *et al.*, Nanoscopic visualization of cross-linking density in polymer networks with diarylethene photoswitches. *Angew. Chem. Int. Ed. Engl.* **57**, 12280–12284 (2018).
42. C. K. Ullal, R. Schmidt, S. W. Hell, A. Egner, Block copolymer nanostructures mapped by far-field optics. *Nano Lett.* **9**, 2497–2500 (2009).
43. Y. Xia, J. A. Kornfield, R. H. Grubbs, Efficient syntheses of brush polymers via living ring opening metathesis polymerization of macromonomers. *Macromolecules* **50**, 3761–3766 (2009).
44. S. C. Radzinski, J. C. Foster, J. B. Matson, Preparation of bottlebrush polymers via a one-pot ring-opening polymerization (rop) and ring-opening metathesis polymerization (romp) grafting-through strategy. *Macromol. Rapid Commun.* **37**, 616–621 (2016).
45. C. J. Ellison, S. D. Kim, D. B. Hall, J. M. Torkelson, Confinement and processing effects on glass transition temperature and physical aging in ultrathin polymer films: Novel fluorescence measurements. *Eur. Phys. J. E Soft Matter* **8**, 155–166 (2002).
46. L. Li *et al.*, Impact of bottlebrush chain architecture on Tg-confinement and fragility-confinement effects enabled by thermo-cleavable bottlebrush polymers synthesized by radical coupling and atom transfer radical polymerization. *J. Polym. Sci.* **58**, 2887–2905 (2020).
47. Z. Qiang, M. Wang, 100th anniversary of macromolecular science viewpoint: Enabling advances in fluorescence microscopy techniques. *ACS Macro Lett.* **9**, 1342–1356 (2020).
48. C. E. Boott *et al.*, In situ visualization of block copolymer self-assembly in organic media by super-resolution fluorescence microscopy. *Chemistry* **21**, 18539–18542 (2015).
49. O. Nevsykyi *et al.*, Fluorescent diarylethene photoswitches - A universal tool for super-resolution microscopy in nanostructured materials. *Small* **14**, 1–12 (2018).
50. Z. Qiang, L. Li, J. M. Torkelson, M. Wang, Determining order-to-disorder transitions in block copolymer thin films using a self-referencing fluorescent probe. *Mol. Syst. Des. Eng.* **5**, 330–338 (2020).
51. G. T. Dempsey, J. C. Vaughan, K. H. Chen, M. Bates, X. Zhuang, Evaluation of fluorophores for optimal performance in localization-based super-resolution imaging. *Nat. Methods* **8**, 1027–1036 (2011).
52. J. Licea-Rodriguez *et al.*, Multicolor fluorescence microscopy using static light sheets and a single-channel detection. *J. Biomed. Opt.* **24**, 1–8 (2019).
53. I. Mitra *et al.*, Thin film phase behavior of bottlebrush/linear polymer blends. *Macromolecules* **47**, 5269–5276 (2014).
54. A. K. Gustavsson, P. N. Petrov, M. Y. Lee, Y. Shechtman, W. E. Moerner, 3D single-molecule super-resolution microscopy with a tilted light sheet. *Nat. Commun.* **9**, 123 (2018).
55. S. R. P. Pavani *et al.*, Three-dimensional, single-molecule fluorescence imaging beyond the diffraction limit by using a double-helix point spread function. *Proc. Natl. Acad. Sci. U.S.A.* **106**, 2995–2999 (2009).
56. J. Baschnagel *et al.*, Semiflexible chains at surfaces: Worm-like chains and beyond. *Polymers (Basel)* **8**, 1–35 (2016).
57. J. Paturej, S. S. Sheiko, S. Panyukov, M. Rubinstein, Molecular structure of bottlebrush polymers in melts. *Sci. Adv.* **2**, e1601478 (2016).
58. H. Liang, Z. Cao, Z. Wang, S. S. Sheiko, A. V. Dobrynin, Combs and bottlebrushes in a melt. *Macromolecules* **50**, 3430–3437 (2017).
59. P. F. Green, The structure of chain end-grafted nanoparticle/homopolymer nanocomposites. *Soft Matter* **7**, 7914–7926 (2011).
60. I. Borukhov, L. Leibler, Enthalpic stabilization of brush-coated particles in a polymer melt. *Macromolecules* **35**, 5171–5182 (2002).
61. R. J. Macfarlane *et al.*, Improving brush polymer infrared one-dimensional photonic crystals via linear polymer additives. *J. Am. Chem. Soc.* **136**, 17374–17377 (2014).
62. A. H. Mah *et al.*, Bottlebrush copolymer additives for immiscible polymer blends. *Macromolecules* **51**, 5665–5675 (2018).
63. B. Duplantier, Exact scaling form for the collapsed 2D polymer phase. *Phys. Rev. Lett.* **71**, 4274 (1993).
64. L. J. Fetters, D. J. Lohse, R. H. Colby, "Chain dimensions and entanglement spacings" in *Physical Properties of Polymers Handbook*, J. E. Mark, Ed. (Springer, New York, NY, 2007), pp. 447–454.
65. P. G. Ferreira, A. Ajdari, L. Leibler, Scaling law for entropic effects at interfaces between grafted layers and polymer melts. *Macromolecules* **31**, 3994–4003 (1998).
66. C. S. Smith, N. Joseph, B. Rieger, K. A. Lidke, Fast, single-molecule localization that achieves theoretically minimum uncertainty. *Nat. Methods* **7**, 373–375 (2010).
67. F. Huang *et al.*, Video-rate nanoscopy using sCMOS camera-specific single-molecule localization algorithms. *Nat. Methods* **10**, 653–658 (2013).
68. F. Huang, S. L. Schwartz, J. M. Byars, K. A. Lidke, Simultaneous multiple-emitter fitting for single molecule super-resolution imaging. *Biomed. Opt. Express* **2**, 1377–1393 (2011).
69. M. Ovsny, P. Krížek, J. Borkovec, Z. Švindrych, G. M. Hagen, ThunderSTORM: A comprehensive ImageJ plug-in for PALM and STORM data analysis and super-resolution imaging. *Bioinformatics* **30**, 2389–2390 (2014).